Comparative Analysis of Methods to Estimate Geodetic Strain Rates from GNSS Data in Italy

Riccardo Nucci[*,1], Enrico Serpelloni[2] , Licia Faenza[2], Alexander Garcia[2],
Maria Elina Belardinelli[1]

[(1)] Dipartimento di Fisica e Astronomia, University of Bologna, Italy
[(2)] Istituto Nazionale di Geofisica e Vulcanologia, Bologna, Italy

Abstract

Our ability to estimate surface deformation rates in the Central Mediterranean has considerably enhanced in the last decade thanks to the growth of continuous Global Navigation Satellite System (GNSS) networks. Focusing on the Apennine/Alpine seismogenic belt, this area offers the opportunity to test the use of geodetic strain rates for constraining active tectonic processes and for seismic hazard assessments. Given the importance of geodetic strain rate models in modern hazard estimation approaches, however, one has to consider that different approaches can provide significantly different strain rate maps. Despite the increasing availability of GNSS velocity data, in fact, strain rate models can significantly differ, because of the spatial heterogeneity of GNSS station locations and inherent strategies in computing strain rates. Using a dense GNSS velocity dataset, this study examines three methods for estimating horizontal strain rates, described in the recent literature, and selected to represent approaches of increasing mathematical complexity. The advantages, drawbacks, and optimal settings of each method are discussed. The main result is an ensemble of strain rate models that enable the evaluation of epistemic uncertainties in seismicity rate models constrained by geodetic velocities.

1. Introduction

The increasing number of continuous Global Navigation Satellite System (GNSS) networks [e.g., Blewitt, Hammond and Kreemer, 2018] significantly improve our ability to resolve deformation rates along active plate boundary zones. Continuous GNSS stations measure the Earth's surface displacement rates with sub-millimeter precision and stations velocities from differently dense networks are commonly used to estimate spatial derivatives of the velocity field, which are associated with tectonic and geodynamic processes. In Italy, the rising density of continuously recording GNSS stations [Devoti et al., 2017 and Serpelloni et al., 2022] enables us to map the surface strain rate during the interseismic phase of the earthquake cycle with unprecedented spatial details. This information is valuable in understanding where and to what extent tectonic deformation accumulates, providing crucial constraints for seismic hazard models.

Generally, Probabilistic Seismic Hazard Analysis (PSHA) aims to combine different types of information, such as seismic catalogs, geological data on active faults and focal mechanisms of past earthquakes, to describe the distribution of future shaking that may occur at a site. Indeed, a fundamental challenge in PSHA is to quantify and integrate various types of uncertainties and models. In Italy, the latest Italian seismic hazard model [Meletti et al., 2021] incorporates two earthquake rate models derived from geodetic strain rate fields. Strain rate models offer a distinct and independent source of information compared to those derived from seismic data, as they are largely independent of the Italian Parametric Earthquake Catalogue [Meletti et al., 2021]. Thus, the development of reliable geodetic models remains an active and significant research challenge, given their importance in hazard estimation. Hence, obtaining robust estimates of the surface geodetic deformation rates, which are representative of the tectonic deformation rates, is fundamental.

On the other hand, the uncertainties in the estimates of geodetic strain rate maps can be relevant despite the growing availability of velocity data. This is mainly due to the non-uniform distribution in space of geodetic station locations [Maurer and Materna, 2023]; therefore, a method to compute strain rates from sparse velocities has to perform, in general, a form of interpolation [Maurer and Materna, 2023]. Moreover, since the strain rate is computed from the first spatial derivatives of the velocity field, its estimate is even more uncertain than that of the velocity field itself.

In this study, a dense GNSS velocity data set for Italy and its surroundings is employed to derive the horizontal strain rate fields using three different methods. These methods encompass some of the most commonly used approaches in the existing recent literature and are chosen as representative of methods of increasing mathematical complexity. The methods used in this study are available in the Strain_2D software [Materna and Maurer, 2023], which allows for the comparison of strain rate models within a common framework. Their respective advantages and disadvantages are examined, together with the optimal parameters' settings for each method. The focus of this study is set on tectonic deformation rates, for their interest in any seismotectonic application and their implications for seismic hazard analysis. The GNSS velocities are filtered to obtain a data set that is free as much as possible from non-tectonic deformation signals. The final objective is to compute strain rate fields representative of the tectonic deformation rates, compare them, and make them available for future research, such as their use in the development of seismicity rate models. Moreover, using an ensemble of plausible models to compute strain rate fields can be useful for analyzing the effect of epistemic uncertainties in the final results.

2. Velocity field from GNSS data

2.1 The GNSS dataset

In this study, we use GNSS velocity data derived by analyzing and processing GNSS observations from more than 4000 GNSS stations from multiple networks operating in Euro-Mediterranean, Eurasian, and African regions following the procedures described in Serpelloni et al. [2022].

The accuracy and precision of linear velocity estimates are influenced by the length of the time series. In their study, Masson, Mazzotti, and Vernant, [2019] utilized statistical analyses on synthetic position time series to evaluate the precision of GNSS velocities, accounting for standard noise, seasonal variations, and position offsets. Their findings suggest that for studies demanding a precision of less than 1 mm/yr, a time series duration of less than 4.5 years is insufficient. As indicated by Serpelloni et al. [2022] apart from semi-annual and annual signals, long-period noise and multi-annual loading signals significantly influence linear velocity estimates and uncertainties. In their research, Serpelloni et al. [2022] analyzed a substantial number of GNSS stations in the Euro-Mediterranean region, each with nearly a complete 12-year observation history. Their findings highlighted that to achieve velocity estimates consistent with those from the entire timespan, a minimum time series length of 6.0 ± 3.6 years for the east and 6.3 ± 2.7 years for the north velocity components is necessary. For this study, to ensure both a dense network of GNSS stations and reliable velocity estimates, only stations with time series lasting at least 4.5 years are considered. This decision aligns with the recommendations from Masson, Mazzotti, and Vernant [2019] and fits within the 95% confidence interval mentioned in Serpelloni et al. [2022].

The focus of this study is on the horizontal velocity data within a region centered around Italy, with latitude ranging from 36° to 48°N and longitude ranging from 5° to 20°E. The velocities are rotated in a Eurasian-fixed reference frame, as defined by the ITRF 2014 [Altamimi et al., 2017]. The resulting velocity includes 1149 stations field and is shown in Figure 1.
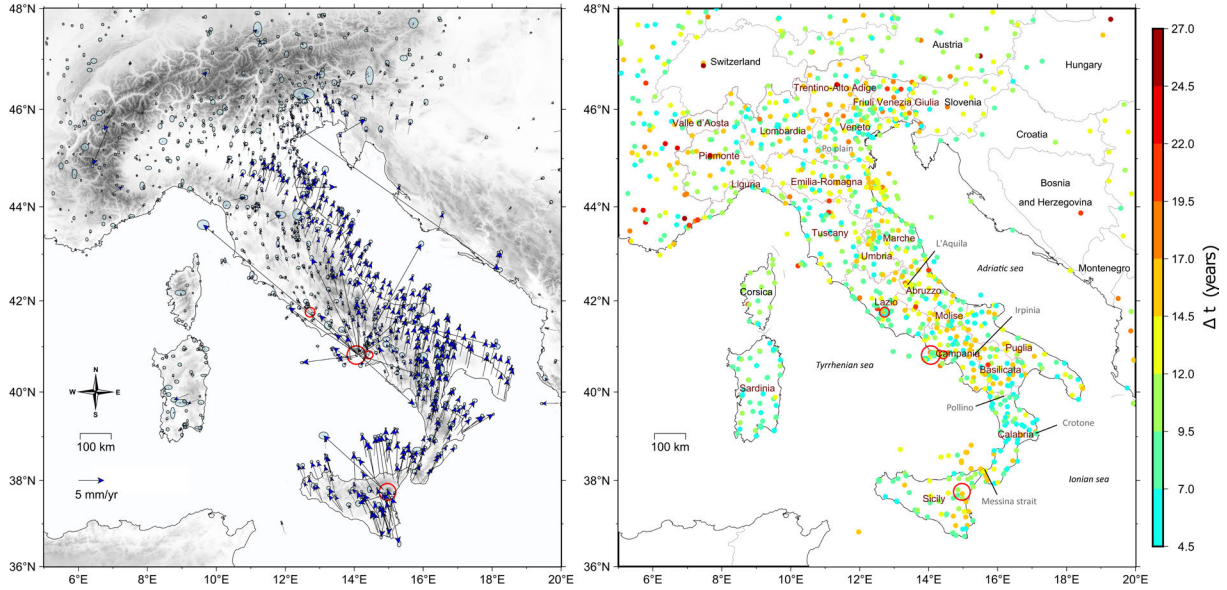
Figure 1. Left: Horizontal GNSS velocity field with 95% error ellipses in a Eurasia fixed reference frame (1149 stations). The plotted data set consists of stations with records longer than 4.5 years in a time window from 1995 to 2023. Circular masks for volcanic areas are also shown (red circles). Right: Stations colored according to the time-series length Δt. The figure also shows labels of regions and zones, part of which are mentioned in the text.

2.2 Filtering and Analysis of the GNSS Velocity Field

The velocity field shown in Figure 1 encompasses signals other than tectonic, including those caused by anthropogenic activity and volcano-tectonic deformation. Additionally, stations in close proximity to each other can exhibit slightly different velocity values due to local conditions, resulting in steep spatial velocity gradients when using numerical algorithms. To address these issues, a filtering procedure is sequentially applied to the overall velocity field through the following steps:

– Gas field exploitation in the northern Adriatic Sea can result in time-varying continuous GPS (CGPS) velocities at offshore stations [Pezzo et al., 2020]. From the dataset, a total of 21 stations located on offshore platforms were excluded based on the nonlinearity of their time series. Specifically, only the A class stations listed in Pezzo et al. [2020] (Table 1) were retained.

– Stations significantly affected by deformation associated with active volcanoes are removed from the dataset. Major areas of influence, including the Vesuvio and Campi Flegrei area, Ischia, the Etna volcano, and the Colli Albani zone, are delimited by circular masks (Figure 1). Stations inside these masks are excluded, resulting in the removal of 43 stations within 4 circular masks.

– Stations located in close proximity to each other (on the order of hundreds of meters) can lead to inaccurate strain rate estimates due to variations in station velocities over short distances. Thus, a weighted mean velocity is calculated for stations closer than 1 km according to:

$$v_i = \frac{\left(\frac{1}{\sigma_{1,i}^2}\right)v_{1,i} + \left(\frac{1}{\sigma_{2,i}^2}\right)v_{2,i}}{\left(\frac{1}{\sigma_{1,i}^2}\right) + \left(\frac{1}{\sigma_{2,i}^2}\right)} \qquad \sigma_i = \frac{1}{\sqrt{\left(\frac{1}{\sigma_{1,i}^2}\right) + \left(\frac{1}{\sigma_{2,i}^2}\right)}} \qquad i = e, n \qquad (1)$$

where v_i and σ_i represent respectively the velocities and the uncertainty of the GNSS stations and e and n refer to the east and north components.

– Finally, in order to identify anomalous velocities, the agreement between the velocity of each station and the velocities of its neighbors is evaluated, employing an approach inspired by the methodology presented in Piña-Valdés et al. [2022]. The rationale behind this evaluation is that the velocity at one station should not
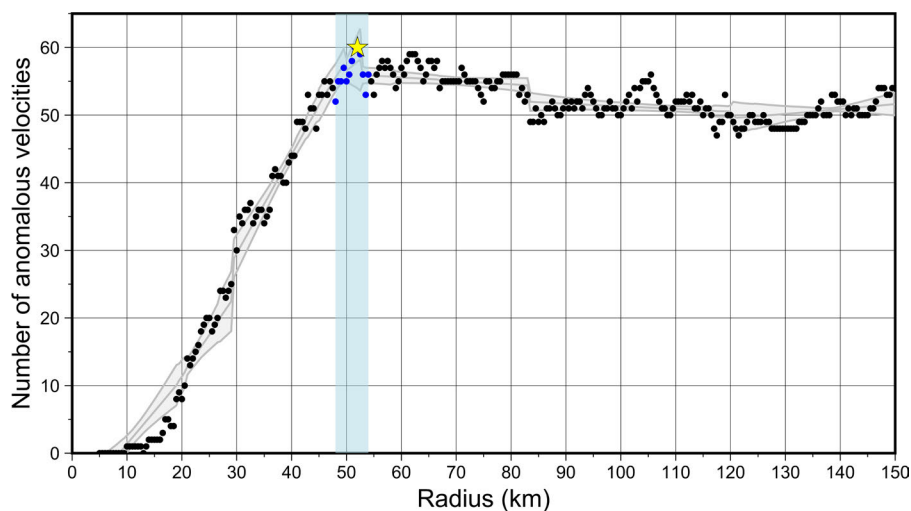
Figure 2. Number of anomalous velocities excluded from the dataset as a function of the radius R. The gray plot shows trend estimate and its 2σ interval. The blue region identifies possible change-points within a 95% confidence interval. Both trend and probable change-points are estimated by employing the Beast software [Zhao et al., 2019]. The star indicates the selected radius and the corresponding number of excluded stations (60).
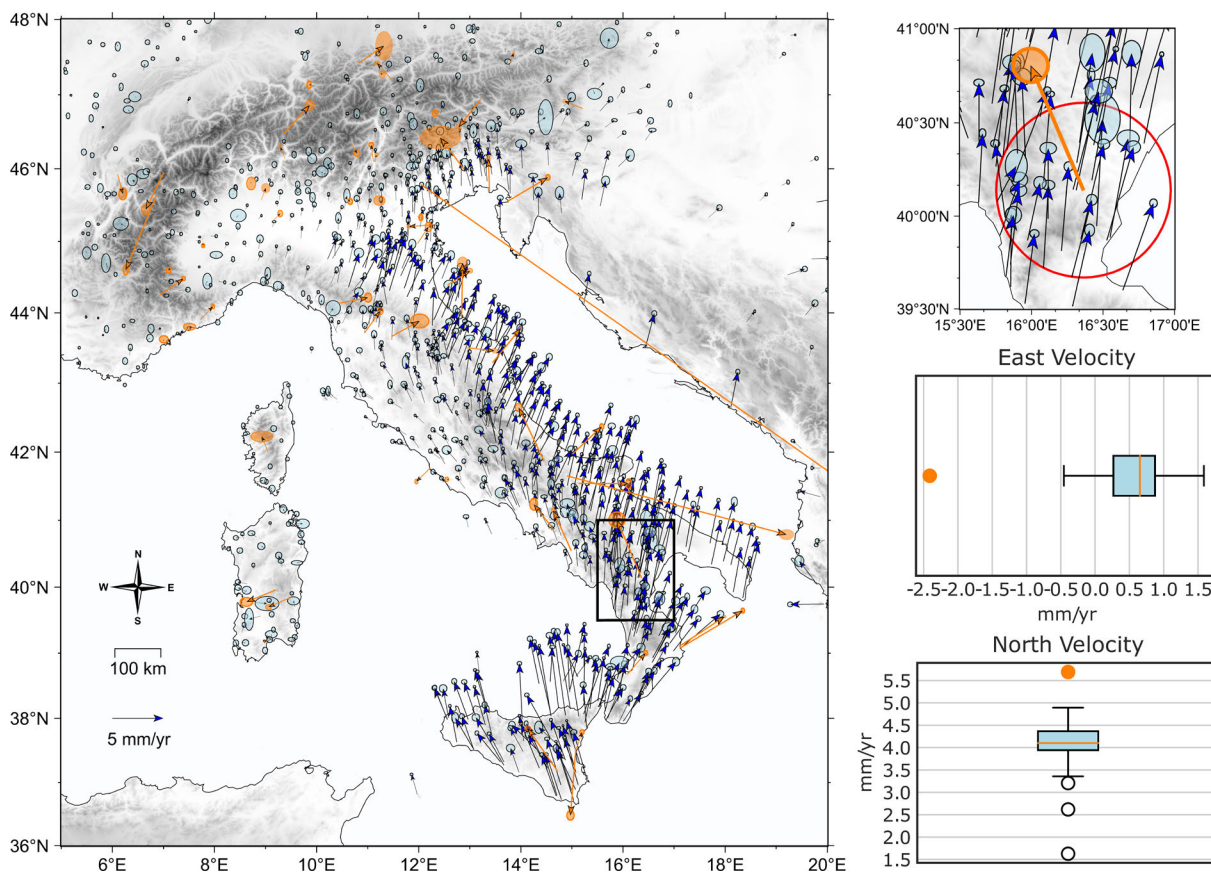

Figure 3. Left plot: Map of the anomalous velocities (orange arrows) of 60 stations detected and removed from the dataset. Stations are denoted as anomalous if they match the condition (2) in more than 50% of the cases in which these stations are considered for the IQR method. Right plot: Detail of an anomalous station and its detection through the IQR method. The red circle has a radius of 52 km. Each boxplot shows the distribution of velocities (on east and north components) inside the red circles in terms of: the median (central line in the box), the interquartile range (box edges), and potential anomalous velocities (points outside the whiskers). Orange points represent the velocity of the anomalous station.
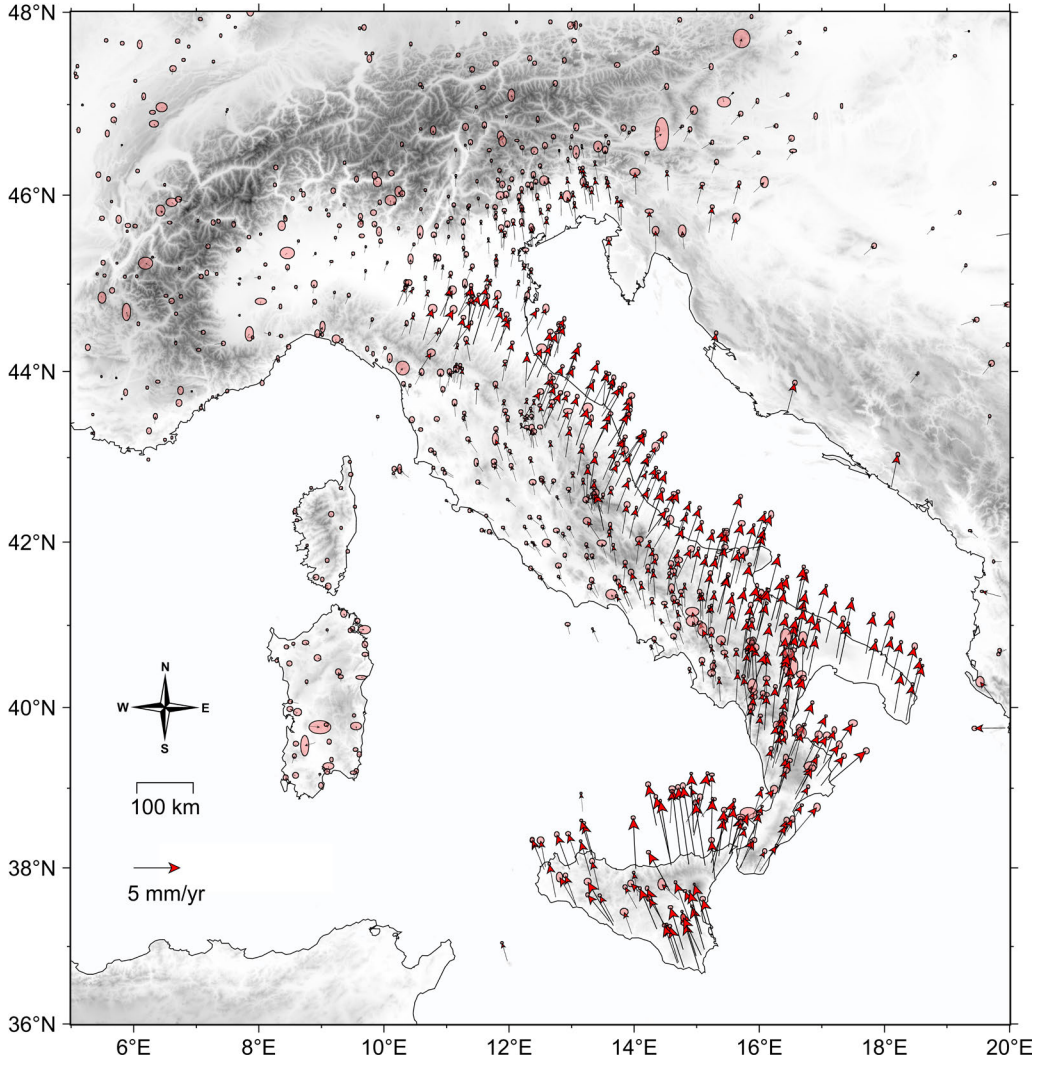
Figure 4. Horizontal GNSS velocity field with 95% error ellipses filtered following the procedure described in this section. The field includes measurements from 928 stations.

differ significantly from the velocities of its neighbors. For each station, a circle centered on it with a radius of R is considered. A station in this area is flagged as a potential anomalous station if at least one of its velocity components falls outside an interval defined by the $1.5 \, IQR$ (InterQuartile Range) rule, computed by considering all stations within the circle. Therefore, a station is flagged as a potential anomalous if it meets the following condition:

$$v_i < q_{1,i} - 1.5 \cdot IQR_i \qquad \text{or} \qquad v_i > q_{3,i} + 1.5 \cdot IQR_i \qquad \text{for} \qquad i = e, n \qquad (2)$$

where $q_{1,i}$ is the first velocity quartile, $q_{3,i}$ is the third velocity quartile and IQR_i is the interquartile range. We decide to exclude from the dataset only the stations that are marked as potential anomalies in more than 50% of the cases in which the station was considered. The selection of the radius R is subject to a certain degree of arbitrariness. A reasonable approach to determine a suitable value for R is to consider a tradeoff between the number of stations removed and the increase in radius (as depicted in the Figure 2). A value of R equal to 52 km is chosen as a satisfactory compromise, as it resides within a region of slope change and maximizes the number of detected anomalous velocities (depicted in Figure 3). This detection leads to exclude 60 stations from the datasets.

The resulting velocity field, obtained after applying these steps, is presented in Figure 4 and consists of 928 velocity vectors.

Riccardo Nucci et al.

3. Geodetic Strain Rate Maps

3.1 The Strain rate tensor

The strain rate tensor is defined from the spatial derivatives of the velocity vector v in a Cartesian reference frame of coordinates x_i:

$$\dot{\varepsilon}_{ij} = \frac{1}{2}\left(\frac{\partial v_i}{\partial x_j} + \frac{\partial v_j}{\partial x_i}\right) \qquad \text{where} \qquad i,j = 1,2,3. \tag{3}$$

The tensor $\dot{\varepsilon}_{ij}$ is a second-order, symmetric tensor, with indices indicating components over three Cartesian axes. In this study, the horizontal components of the surface velocity data are considered and then $\dot{\varepsilon}_{ij}$ is a purely 2D tensor with $i,j = 1,2$. Henceforth, the term *strain rate* will refer to the 2D version of (3).

In the subsequent sections, scalar fields derived from the strain rate will be plotted and compared. These fields include the first invariant and the second invariant of the strain rate, defined as:

$$D = \dot{\varepsilon}_{11} + \dot{\varepsilon}_{22}, \tag{4}$$

$$I_2 = \sqrt{\dot{\varepsilon}_{11}^2 + \dot{\varepsilon}_{22}^2 + 2\dot{\varepsilon}_{12}^2}. \tag{5}$$

D is also known as dilatation rate while I_2 represents the Frobenius norm [Golub and Van Loan, 1989] of the strain rate tensor and can be considered a measure of the overall magnitude of the strain rate. The strain rate and its first and second invariants have dimensions of inverse time and will be shown in plots in units of $10^{-9}/yr$, also denoted as $nstr/yr$.

From the strain rate tensor, it is possible to compute its principal axes by solving the eigenvalues and eigenvectors problem:

$$\dot{\varepsilon}_{ij}u_j = \lambda\,u_i, \tag{6}$$

where Einstein's notation over repeated indices is used. As the strain rate is a real, 2D, and symmetrical matrix, the eigenvalues can be simply computed as:

$$\lambda_1, \lambda_2 = \frac{1}{2}\left[(\dot{\varepsilon}_{11} + \dot{\varepsilon}_{22}) \pm \sqrt{(\dot{\varepsilon}_{11} - \dot{\varepsilon}_{22})^2 + 4\dot{\varepsilon}_{12}^2}\right], \tag{7}$$

where the solution with the + sign corresponds to the maximum expansion, and the solution with the – sign corresponds to the maximum compression. The eigenvectors are mutually orthogonal due to the symmetry of $\dot{\varepsilon}_{ij}$ and the directions relative to maximum shear are located at 45° with respect to the principal axes.

3.2 Characterization of the strain rate solutions

Each method for the computation of the geodetic strain rate is characterized by a variability in the results that depends mainly on how the method's parameters are tuned. Tuning the parameters can lead to models that are smoother or rougher and that fit the GNSS velocity data well or less well. In order to quantify these characteristics, the following definitions are then introduced:

- In order to quantify the roughness of the strain rate fields, intended as a measure of the spatial variability of the second invariant of the strain rate, the root mean squared gradient of the second invariant I_2 is introduced:

$$\sigma_s = \left(\frac{1}{A} \int_A [\nabla I_2]^2 dA \right)^{1/2},\tag{8}$$

where A is the area of the investigated region. The rationale is that a nearly constant I_2 field should lead to σ_s approaching zero, while a field with great spatial gradients should result in a greater σ_s. In order to compare the strain rate variability of different strain rate maps within each method, σ_s is computed for maps with the same grid spacing of 0.025° in longitude and latitude.

- In this study, the adopted approaches provide a modeled velocity field together with the associated strain rate field. To quantify the goodness of fit with GNSS velocities for each method, the Root Mean Squared Error (RMSE) and Weighted Root Mean Squared Error (WRMSE) are evaluated, defined respectively as:

$$RMSE = \left\{ \frac{1}{2N_s} \sum_{i=1}^{N_s} \left[\left(v_{i,e}^{obs} - v_{i,e}^{mod} \right)^2 + \left(v_{i,n}^{obs} - v_{i,n}^{mod} \right)^2 \right] \right\}^{1/2},\tag{9}$$

$$WRMSE = \left\{ \frac{\sum_{i=1}^{N_s} \left[w_{i,e} \left(v_{i,e}^{obs} - v_{i,e}^{mod} \right)^2 + w_{i,n} \left(v_{i,n}^{obs} - v_{i,n}^{mod} \right)^2 \right]}{\sum_{i=1}^{N_s} \left(w_{i,e} + w_{i,n} \right)} \right\}^{1/2},\tag{10}$$

where $v_{e/n}^{obs/mod}$ are the velocity, observed or modeled, in the east or north direction, the sums are intended over all the N_s stations and the weights are the squared inverse of the uncertainty on velocities: $w_i = 1/(\sigma_i)^2$.

3.3 Nearest Neighbor approach

The Nearest Neighbor approach described by Handwerger et al. [2019] is a weighted nearest neighbor algorithm, implemented in the Strain_2D software [Materna and Maurer, 2023]. This approach estimates both a velocity field and a strain rate field by considering a specified number, N, of the nearest stations within a moving circular window. The method executes a local linear regression without applying any additional weights to the data [Maurer and Materna, 2023] and the computations are bypassed if there are not N stations within the window. As the window's radius acts as a threshold distance, subsequent analyses will vary only the number of stations, maintaining an arbitrarily large radius to enable strain rate estimation throughout the entire region.

The results of this method differ based on the number of neighboring stations considered. Specifically, a larger number of stations results in a spatially smoother strain rate field. The estimated results of the second invariant of the strain rate (equation (5)) for different N (specifically, 12, 18, and 24) are depicted in Figure 5.

The resulting strain rate fields contain some artifacts in the geometry of the strain rate areas that reflect the disposition of the GNSS stations. When smaller values of N are considered, the second invariant exhibits higher spatial concentration along the Apennines and in northern Sicily (as seen at the top of Figure 5). Furthermore, for smaller N, the resulting field is progressively more sensitive to local gradients of the velocity field, leading to strain rate spots in locations such as the northwest Apennines, the Adriatic Sea, and the eastern Calabrian Arch. On the other hand, the residuals are larger when considering larger values of N, as shown at the bottom of Figure 5. The orientation of the residuals, however, does not exhibit systematic patterns with higher values of N, except for a slight increase in residuals with a northern direction. This increase is partially due to the misfit in Sicily, where higher residuals are concentrated. Indeed, a strong velocity gradient exists when transitioning from continental Sicily to the Aeolian Islands [Mastrolembo Ventura et al., 2014] that is accurately modeled only for lower values of N.

Despite its simplicity, this Nearest Neighbor approach fits the GNSS velocity data reasonably well (90% of residuals below 1 mm/yr for the tested values of N) and requires only the setting of a number of nearest neighbor stations. However, there are two primary limitations to the current method. First, it fails to consider the spatial
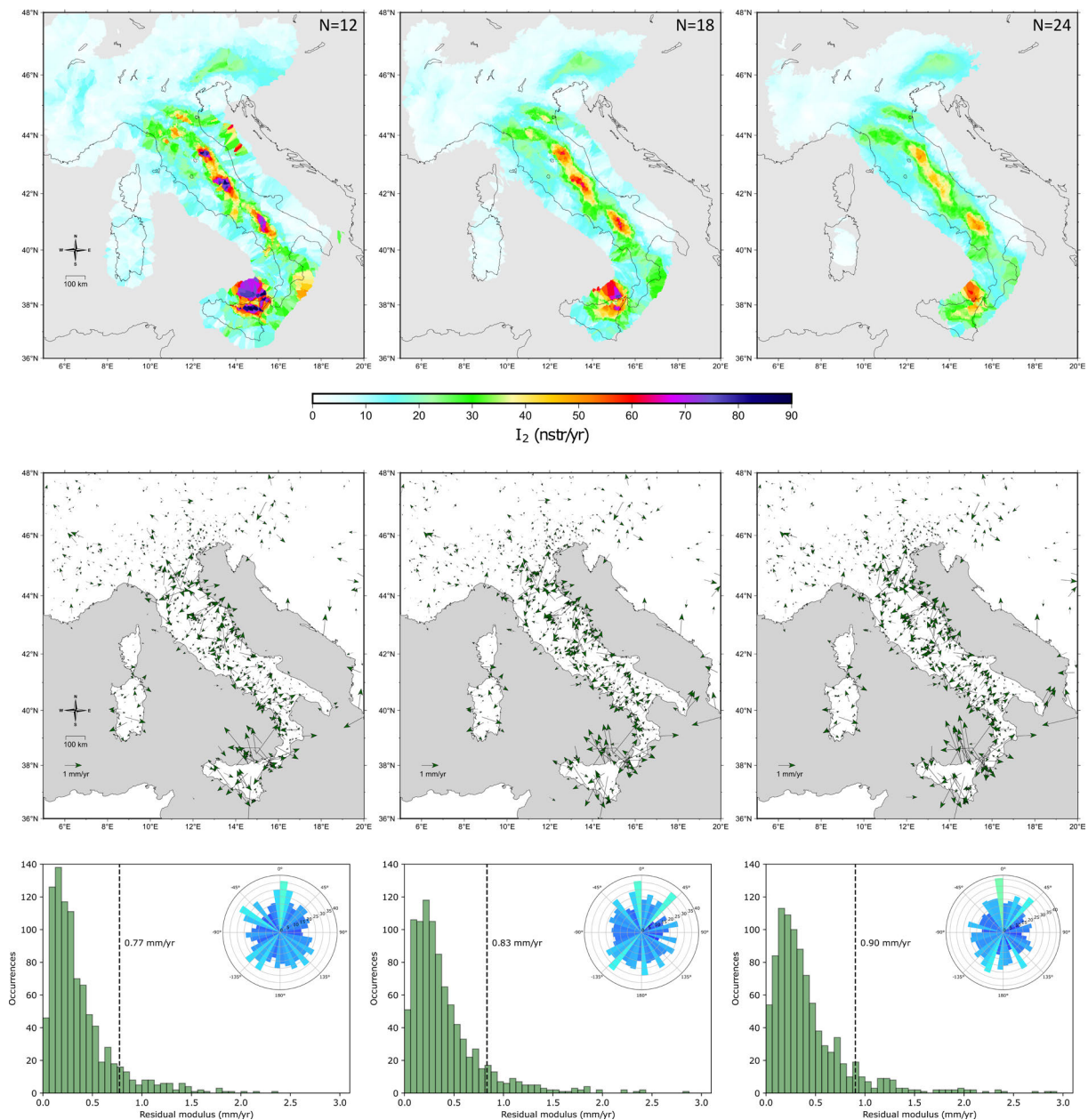
Figure 5. Nearest Neighbor method. From left to right: results relative to different values of the station's number *N*, respectively 12,18,24. Top row: second invariant of the strain rate. Middle row: residual velocity field. Bottom row: histogram of the residual modulus distribution (dashed line shows the 90° percentile) and orientation distribution of the residual velocity field with respect to the north (blue circular histogram). Regions with distances of more than 100 km between stations are masked.

coverage of GNSS station locations, as it always uses the nearest *N* stations for calculating strain rate at every grid point. The second limitation is that the spatial position of the strain rate gradients nearly reflects the spatial disposition of GNSS stations. The other methods outlined in the following paragraphs can fix these limitations, at least to some extent.

3.4 VISR algorithm

The Velocity Interpolation for Strain Rate (VISR) algorithm of Shen et al. [2015] is a weighted neighborhood method for the computation of the strain rate, which is largely used in the recent literature [e.g., for the Euro-Mediterranean

region, England, Houseman, and Nocquet, 2016, Sparacino et al., 2020, Piña-Valdés et al., 2022, Billi et al., 2023].
In the following, a brief overview of the algorithm, following the notation in Shen et al. [2015], is provided (for
further details the reader is ad dressed to the original paper). The algorithm approximates the velocity field at each
interpolation site as the sum of three contributions: a rigid block translation rate, a rotation rate and a strain rate.
The strain rate field parameters are determined through a weighted least-square inversion on neighboring velocities
and the weights on velocities depend on the data uncertainty plus a weighting scheme based on their distances from
the interpolation site and their spatial coverage. Specifically, the diagonal terms of the weighting matrix of velocity
uncertainties (the inverse of the covariance matrix) are multiplied by two functions that depend on distance and
spatial coverage, respectively. The distance weighting function can take two alternative forms:

$$L_i = \exp\left(-\Delta R_i{}^2/D^2\right) \qquad \text{or} \qquad L_i = 1/\left(1 + \Delta R_i{}^2/D^2\right) \qquad (11)$$

The first is a Gaussian while the second is a quadratic function; both depend on the distance ΔR_i of the interpolation
site from the $i-th$ station and a smoothing parameter D. Also, the spatial coverage weighting functions can have two
alternative forms, one of azimuthal weighting, giving more weight at stations having greater azimuthal coverage
with respect to the interpolation site, and one based on Voronoi cells, giving more weight to stations having a bigger
area of the Voronoi cell where it is located (Figure 6 left).

Given the sum W of the total reweighting coefficients of the data as a function of the smoothing parameter D,
D is automatically determined by the algorithm from the equation $W(D) = W_t$ where W_t is an a-priori and user-
defined weighting threshold. In this way the smoothing parameter D is determined by the data density: the denser
the station array is, the smaller D is, given a certain weighting threshold W_t. In the right of Figure 6, the D values for
a $W_t = 10$ and a weighting scheme composed by Gaussian and Voronoi weighting functions are shown. D values can
be then considered a proxy of station density. The highest density of GNSS stations, and then of smaller D values,
is located along the Apennines and in the north-east part of the Po Valley, while lower station density is present in
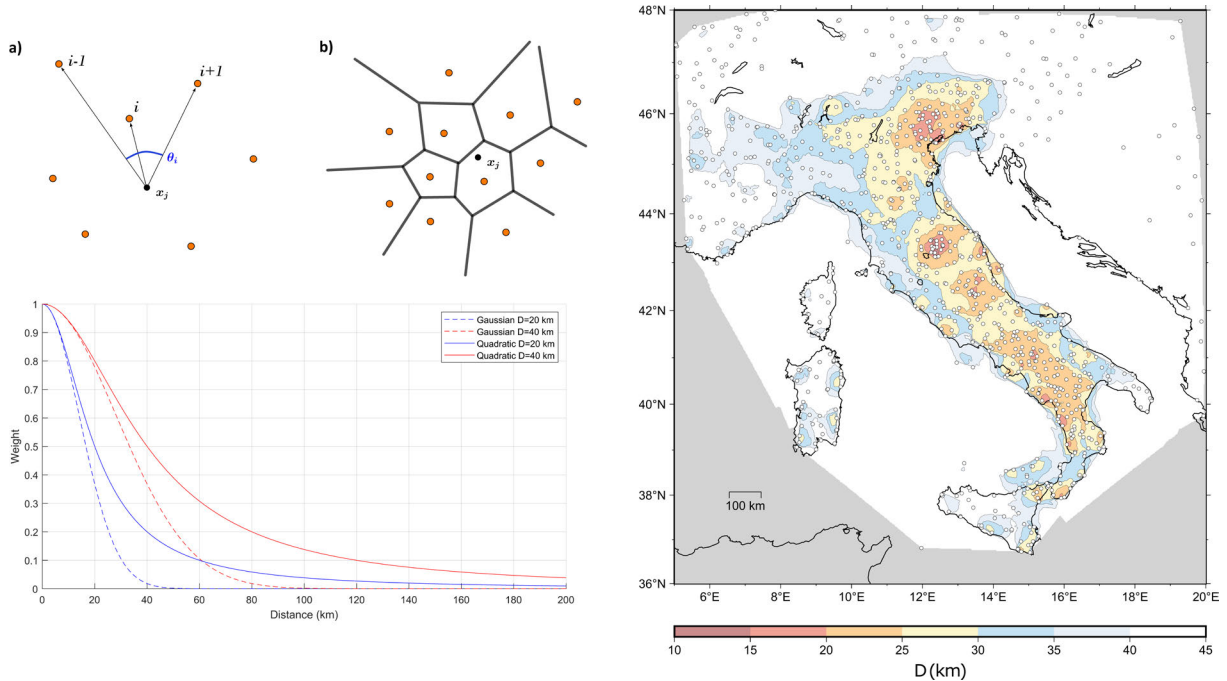the western part of the Po Valley, in Sicily and Sardinia.

Figure 6. Left: Azimuthal weighting scheme in which the contribution of the $i-th$ station is proportional to the angle θ_i (a),
Voronoi weighting scheme in which the weight of each station is proportional to the Area of its Voronoi cell
(b) distance weighting functions for different D values (lower plot). Right: selected smoothing parameter D for
a weighting threshold of 10 and stations' (white dots) distribution.

The primary differences between the second invariant maps, given the variation in weighting schemes, are exemplified in Figure 7.
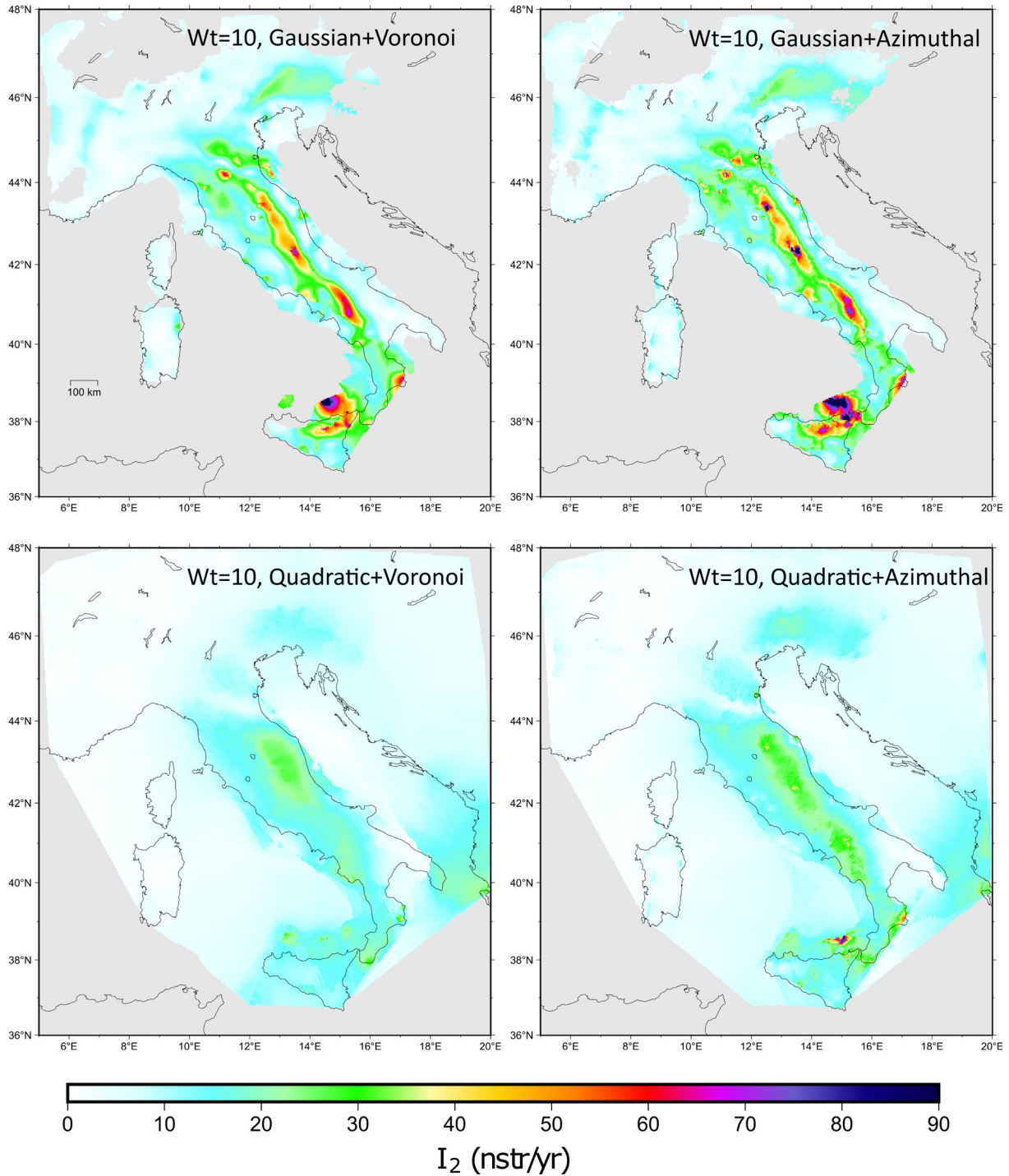

Figure 7. VISR algorithm: second invariant of the strain rate for different weighting schemes (considering $W_t = 10$). Upper left: Gaussian + Voronoi weighting. Upper right: Gaussian + Azimuthal weighting. Bottom left: Quadratic + Voronoi weighting. Bottom right: Quadratic + Azimuthal weighting.

Here, a common weighting threshold of 10 is utilized, but the weighting scheme is varied. From the figures, it can be observed that a Gaussian distance for weighting tends to concentrate more the strain in space with respect to the Quadratic distance (top vs bottom in Figure 7), which is in fact more conservative according to the authors of

the method. Given the good spatial density of GNSS stations in Italy, a Gaussian weight might be a more appropriate weighting scheme. Regarding the spatial coverage weighting scheme, the azimuthal approach generates solutions similar to the Voronoi weighting scheme, but the former presents higher spatial discontinuity of the strain rate than the latter (right vs left in Figure 7). Furthermore, since the Voronoi scheme takes into account a 2D spatial coverage, it could be retained more suitable for computing the strain rate. As a result of these considerations, in the following, the Gaussian + Voronoi weighting scheme will be considered in order to compute the strain rate field.

The results of the second invariant field, using different weighting thresholds, are summarized in Figure 8. As W_t increases, the solution for the second invariant becomes spatially smoother and the fit with the data deteriorates (as seen from the bottom row in Figure 8). This decline in the fit leads to greater modules of residual velocities. The orientation of residuals also depends on the weighting threshold, skewing more "N-S" for the weighting threshold
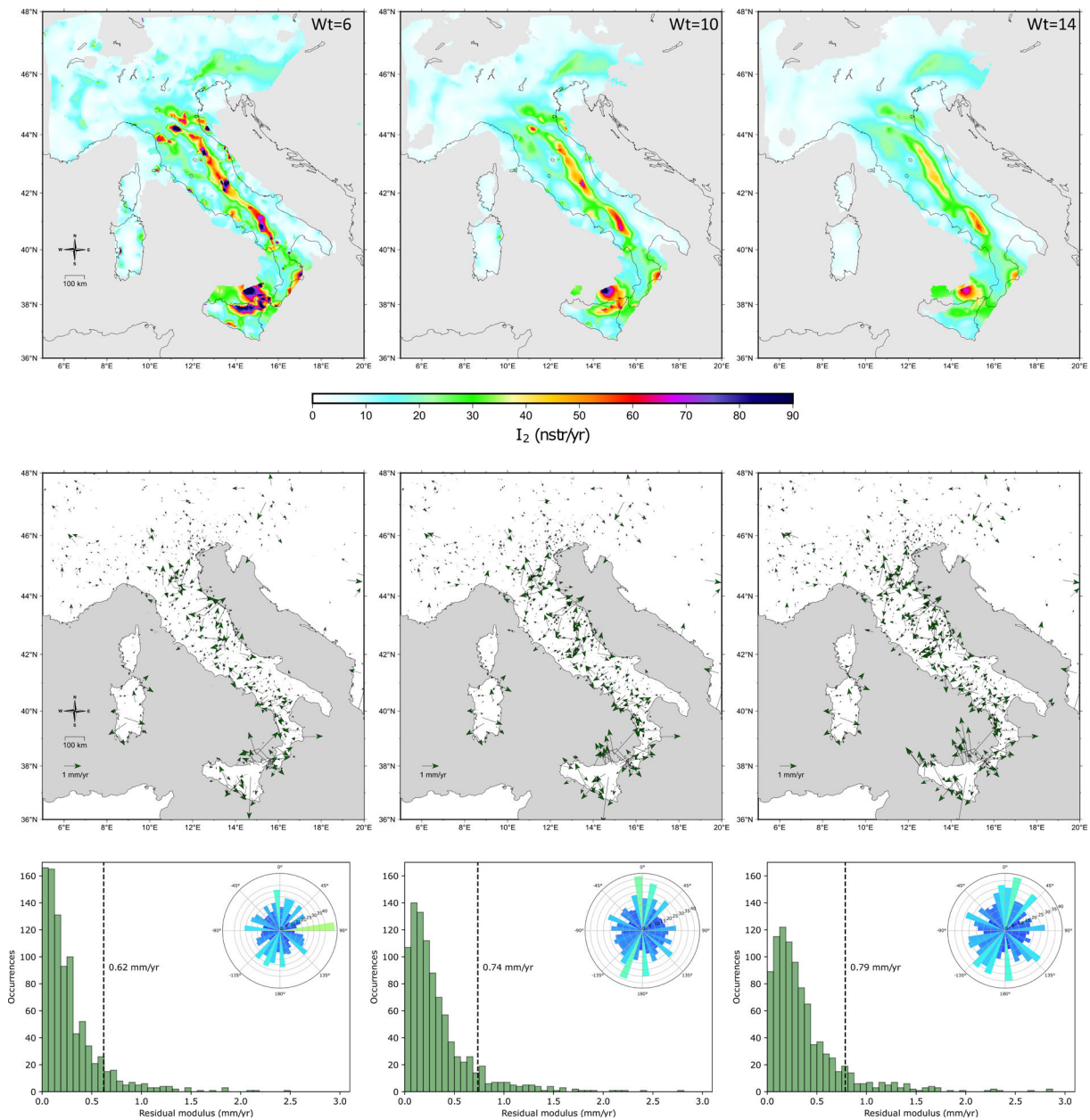

Figure 8. VISR algorithm. From left to right: results relative to different values of the weighting threshold W_t, respectively 6,10,14. Top row: second invariant of the strain rate. Middle row: residual velocity field. Bottom row: histogram of the residual modulus distribution (dashed line shows the 90° percentile) and orientation distribution of the residual velocity field with respect to the north (blue circular histogram). Regions with D values equal to or larger than 50 km are masked.

of 10 and 14. This is likely because the fit of the velocities in Sicily worsens, leading to a larger N-S component in the residual velocities (as also observed for the Nearest Neighbor approach). Compared to the previous Nearest Neighbor method, the residuals are smaller, and the strain rate belt is more spatially localized along the Apennines and in northern Sicily.

One of the advantages of the VISR algorithm is that it takes into account the spatial density and coverage of GNSS stations when computing the strain rate. However, the method seems to be not very robust at low weighting threshold W_t, where small spots of localized strain rate appear.

3.5 Wavelet-based method

The Wavelet-based method from Tape et al. [2009] involves estimating a continuous spatial velocity field using an expansion of frame functions, specifically a class of wavelets on a sphere. The positions and scales of the wavelets are discrete and labeled by an integer index q. Greater q means denser distribution in space and smaller dimension of the corresponding wavelets (Figure 9). The parameters of this expansion are estimated by solving a least-square problem on the velocity dataset regularized by the norm of the model gradient and adopting regularization parameters chosen by ordinary cross-validation [Tape et al., 2009].
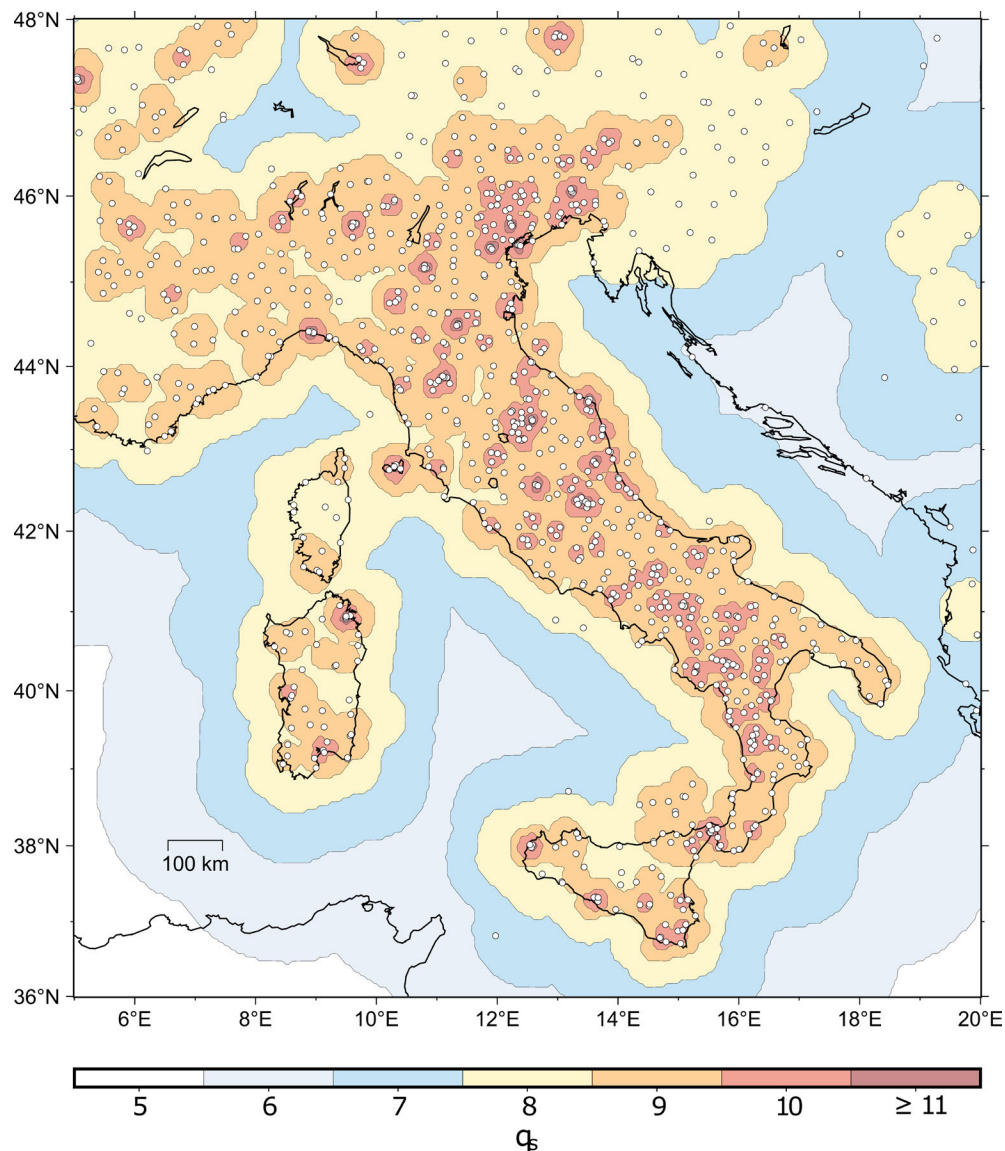

Figure 9. Maximum significant value of the q parameter (q_s) and stations' distribution (white dots).

The relevance of the total velocity field of wavelets corresponding to a certain q depends on the local spatial density of stations. In general, wavelets having greater values of q provide a significant contribution to the expansion where stations are denser in space. Here it is intended as significant a wavelet that has at least three stations inside its first zero crossing. A map of the maximum value of q (q_s), for which the contribution of the corresponding wavelets is significant, is shown in Figure 9. The map can be also considered a proxy for stations' density and is possible to notice that:

- A value of $q_s = 8$, corresponding to a spatial support (distance to the first zero-crossing) of the wavelets of 43.6 km, is available for the entire peninsula.
- A value of $q_s = 9$, corresponding to a spatial support of 21.8 km, is available for a large portion of the region of interest but are excluded: the central northern part of Sicily, some areas in the central Sardinia and the western part of the Po Valley.
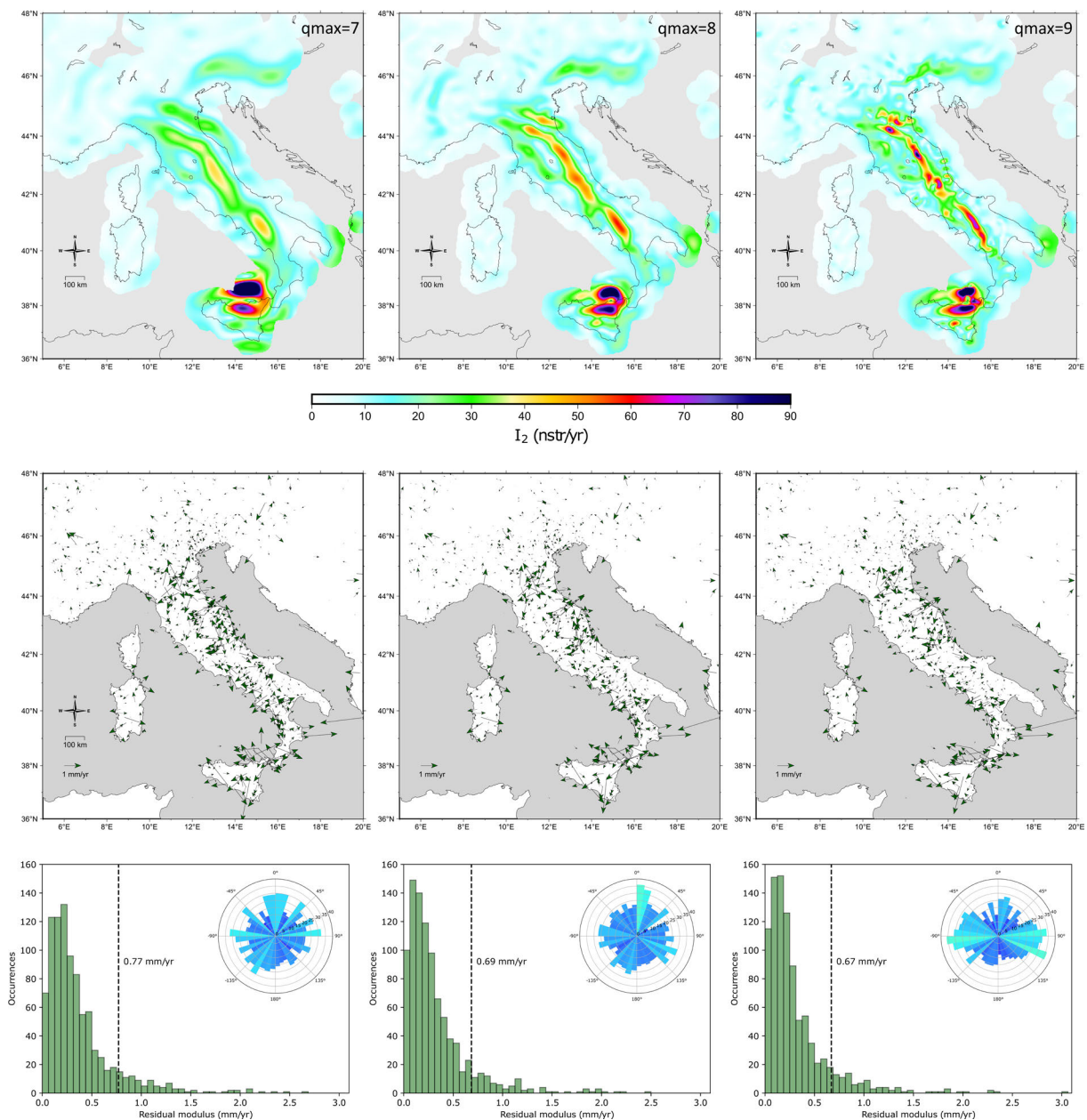

Figure 1. Figure 10 Wavelet-based method. From left to right: results relative to different values of the q_{max} parameter, respectively 7,8,9. Top row: second invariant of the strain rate. Middle row: residual velocity field. Bottom row: histogram of the residual modulus distribution (dashed line shows the 90° percentile) and orientation distribution of the residual velocity field with respect to the north (blue circular histogram). Regions with q_s equal to or smaller than 7 are masked.

– Values of $q_s \geq 10$ (wavelets' spatial support equal or less than 11.4 km) are possible only in stations' clusters unevenly distributed.

We generated different maps using all the wavelets up to a value q_{max}. It is intended that in regions in which $q_s < q_{max}$ the wavelets having indices between q_s and q_{max} will have low contribution to the overall expansion. The choice of the q_{max} parameter is equivalent to the choice of a minimum spatial scale linked to the strain rate variability. Figure 10 shows the resulting scalar fields for the second invariant of the strain rate for $q_{max} = 7,8,9$ computed from numerical derivatives on the resulting estimated velocity field. The resulting strain rate maps are different in the
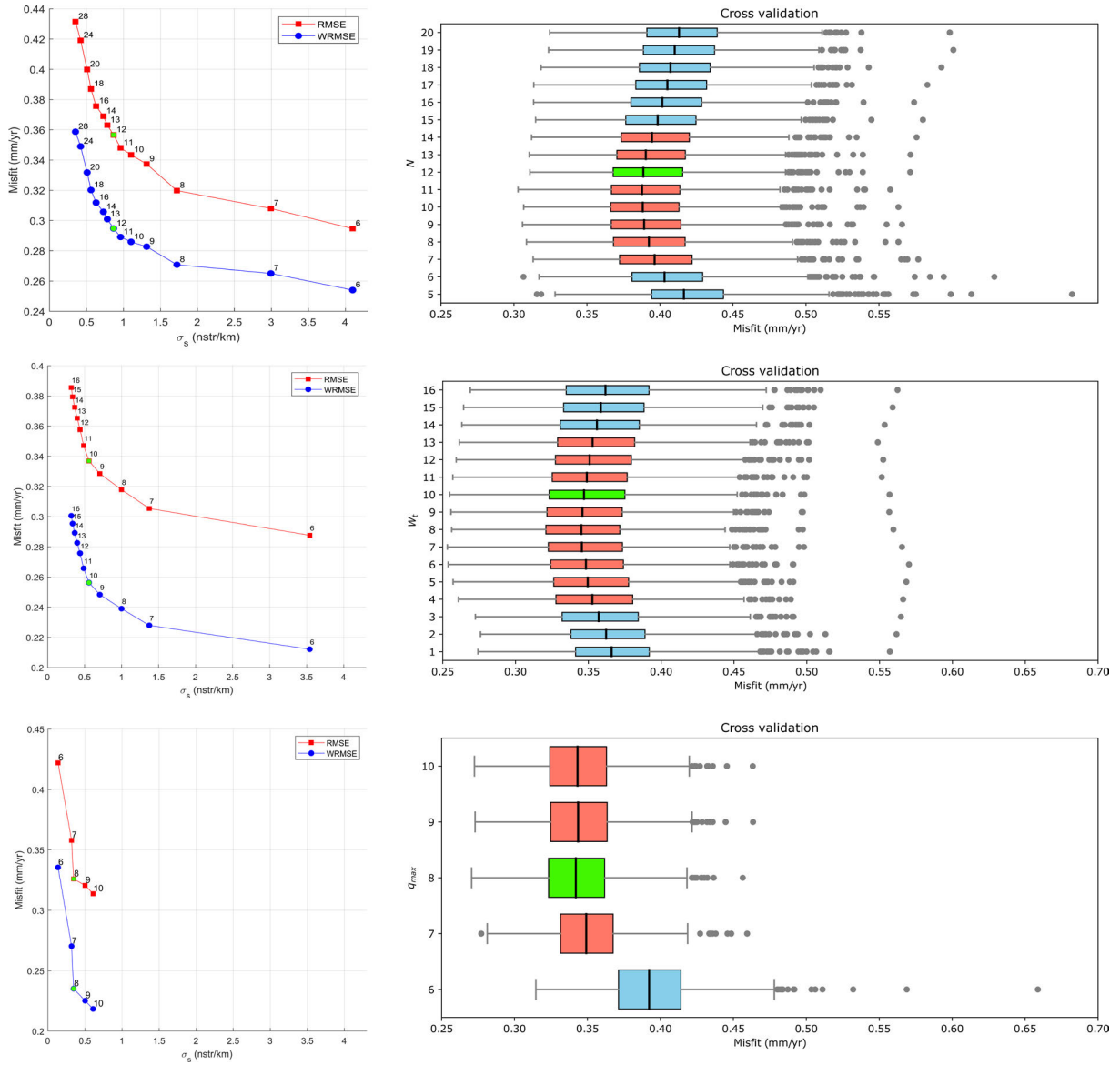
Figure 11. Left Plots: Tradeoff between misfit in terms of RMSE (red) and WRMSE (blue) (from equations (9) and (10)) and σ_s (from equation (8)) for three methods. In descending order: Nearest Neighbor, VISR, and Wavelet-based approach. The numbers next to the points in the left plots represent the N parameter for the Nearest Neighbor approach, the W_t for VISR, and the q_{max} for the Wavelet-based approach. Right Plots: Boxplots illustrating the distributions from 1000 Monte Carlo cross-validation iterations. The horizontal axis assesses the misfit using WRMSE, while the vertical axis indicates the method's parameters. Each boxplot showcases the median (central line in the box), the interquartile range (box edges), and potential outliers (points outside the whiskers). Red boxes indicate a distance from the minimum of less than 0.01 mm/yr based on medians. Preferred solutions (highlighted in green) are chosen to be close to the minimum of the cross-validation curve and in the corner of the misfit plots.

way strain rate is concentrated in space (more localized for high q_{max} values) and in the mean strain values (higher for high q_{max} values). The fit results appear instead similar and in fact, the 90° percentiles of modulus velocity are very close to each other. The orientation of residuals for $q_{max} = 9$ shows a prevalent W-E trend (probably in part due to the difficulties in fitting the W-E components of velocities in Sicily and Calabria). The method seems to be more robust to potential outliers than the VISR since small spots of localized strain appear only for high q_{max} (equal or greater than 9), corresponding to small spatial scales of interest.

3.6 Tuning of the models' parameters

In the previous sections, we show how the results vary using different algorithms for the computation of the strain rate. In addition to the choice of the strain rate computation method, each method has its own variability in the results that depends on how the parameters of each method are tuned.

The selection of a proper parameter setting is not straightforward. Ideally, one should aim at a balance between goodness of fit and smoothing of the results, to avoid abrupt, unrealistic (from a tectonic perspective), changes in the strain rate field. The key parameters to be set include the number of stations N for the Nearest Neighbor approach, the weighting threshold W_t for the VISR method, and the index q_{max} for the Wavelet-based method.

– The relationship between the spatial variability of strain rates and goodness of fit is evaluated by plotting the RMSE or WRMSE in equations (9), (10) against the strain rate variability in equation (8). A good parameter choice corresponds to a solution in the corner point on this plot (Figure 11 left).

– The fit performances of each method are assessed using Monte Carlo cross-validation, with varying parameters [refer to Berrar, 2019 for a description of cross-validation techniques]. The 70% of the velocity dataset is used to compute the strain rate (training set) while the remainder is used to validate the results by analyzing the misfit on this remaining part (test set). The partition between the training and test set is randomly chosen and performed a thousand times. The solution that fits best unseen data stands in the minimum of the misfit curves resulting from all iterations.

The results of these approaches and the selected parameters for the three methods are shown in Figure 11. The arbitrariness of parameter choice is mitigated by selecting parameters that correspond to a solution at a corner of the spatial variability versus misfit plot and near the absolute minimum of the cross-validation curve.

4. Results

In general, the spatial distribution and density of the GNSS stations determine the maximum spatial resolution attainable for the strain rate models. For the VISR and Wavelet-based methods, the inversion details rely on the station's spatial density. As mentioned earlier, Figure 6 and Figure 9 can both serve as indicators of station density. The comparison of the two maps reveals four areas with increased station density. One of them covers a significant portion of the Umbria-Marche regions in the northern Apennines, another is centered around L'Aquila in the central Apennines, a third spans the southern Apennines in Campania and Basilicata, and the fourth encompasses the southern Alps and northeastern Italy. In these regions, the models' resolution can be enhanced by selecting appropriate parameters. The chosen parameters, discussed in the previous section, were determined by evaluating the strain rate field results on a national scale (section 3.6); however, when evaluating strain rates in smaller regions, characterized by a higher station density, it may be beneficial to revisit the analysis of parameter choices in order to identify parameters more suitable for that specific scale. For example, this could result in selecting a lower W_t and a higher q_{max} for both the VISR and Wavelet-based algorithms. For the Nearest Neighbor approach, opting for a smaller N might produce strain rate solutions that vary over shorter length scales.

The preferred strain rate solutions corresponding to three methods, after selecting the more appropriate parameters, are plotted as dilatation rates (equation (4)) and principal strain rate axes (equation (7)) in Figure 12. Figure 13 displays, instead, cross sections where station velocities and the second invariant of strain rate are projected along the different profiles.

The three maps referenced in Figure 12 highlight several consistent major features. Each map confirms the presence of a unique arch-shaped extensional belt in the Western Alps (with dilatation rates below 20 nstr/yr)
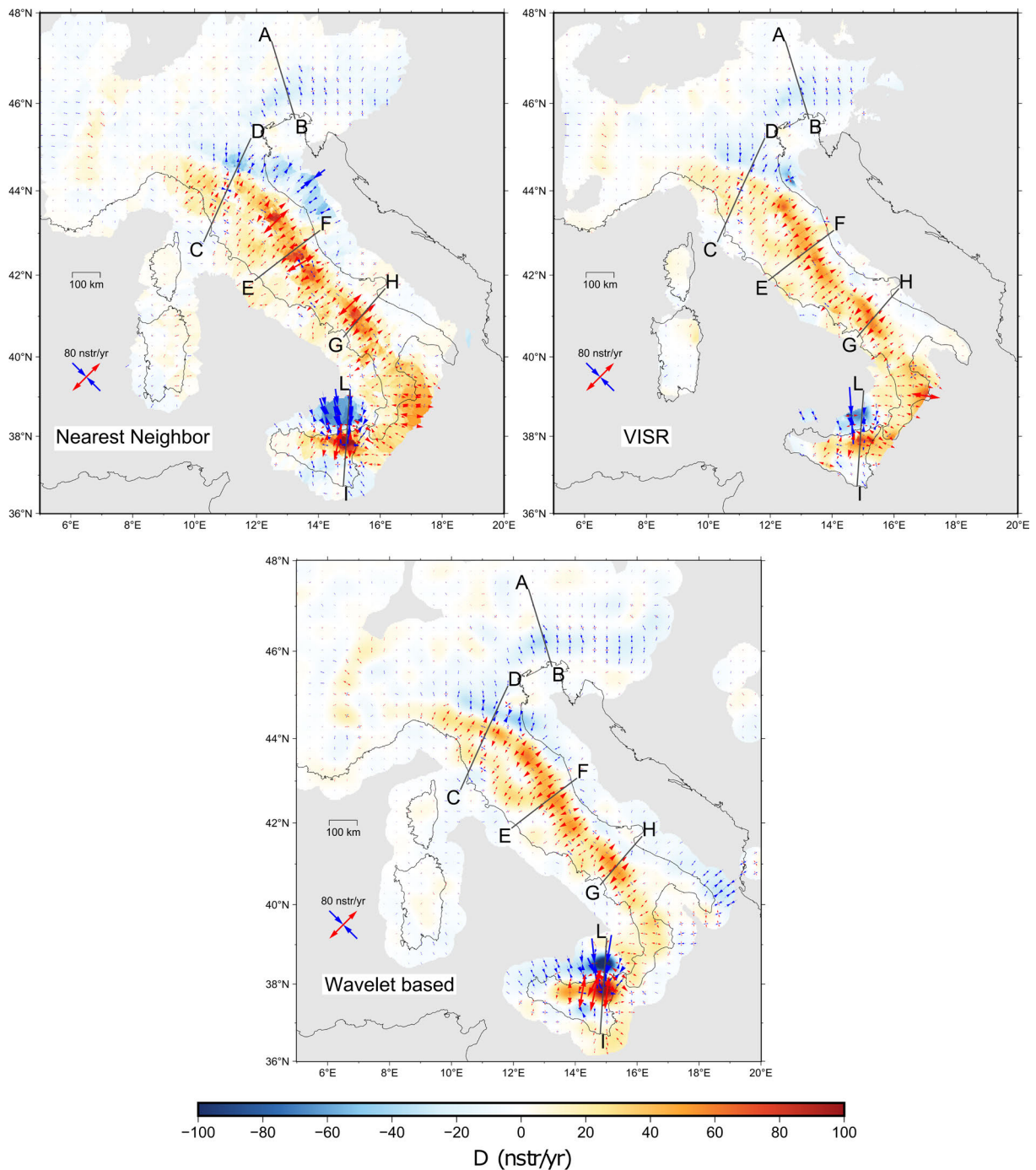
Figure 12. Dilatation rates and principal strain rates axes for the three employed methods.

running perpendicular to the mountain range. Additionally, there is a widespread compressional belt in the South-Eastern Alps with compressional axes oriented in N-S and NW-SE directions and dilatation rates up to about 30 nstr/yr as the absolute maximum value.

Both the northern Apennines' forefront and the Emilian plain display a compressional zone where the axes are primarily oriented N-S to NE-SW and the second invariant of the strain rate is up to about 40 nstr/yr. Along the Apennines, there is a clear unidirectional extensional belt, evident in all three maps. The highest deformation values are located across the Umbria-Marche and in southern Italy (about 50-60 nstr/yr of the second invariant of the strain rate), especially around the Irpinia area (where the second invariant can be greater than 60 nstr/yr).

Distinctly, another extensional deformation belt, located further west compared to the Apennine mountain belt, is noticeable. This belt seems to be set apart from the Apennine belt, especially in places like northern Tuscany.
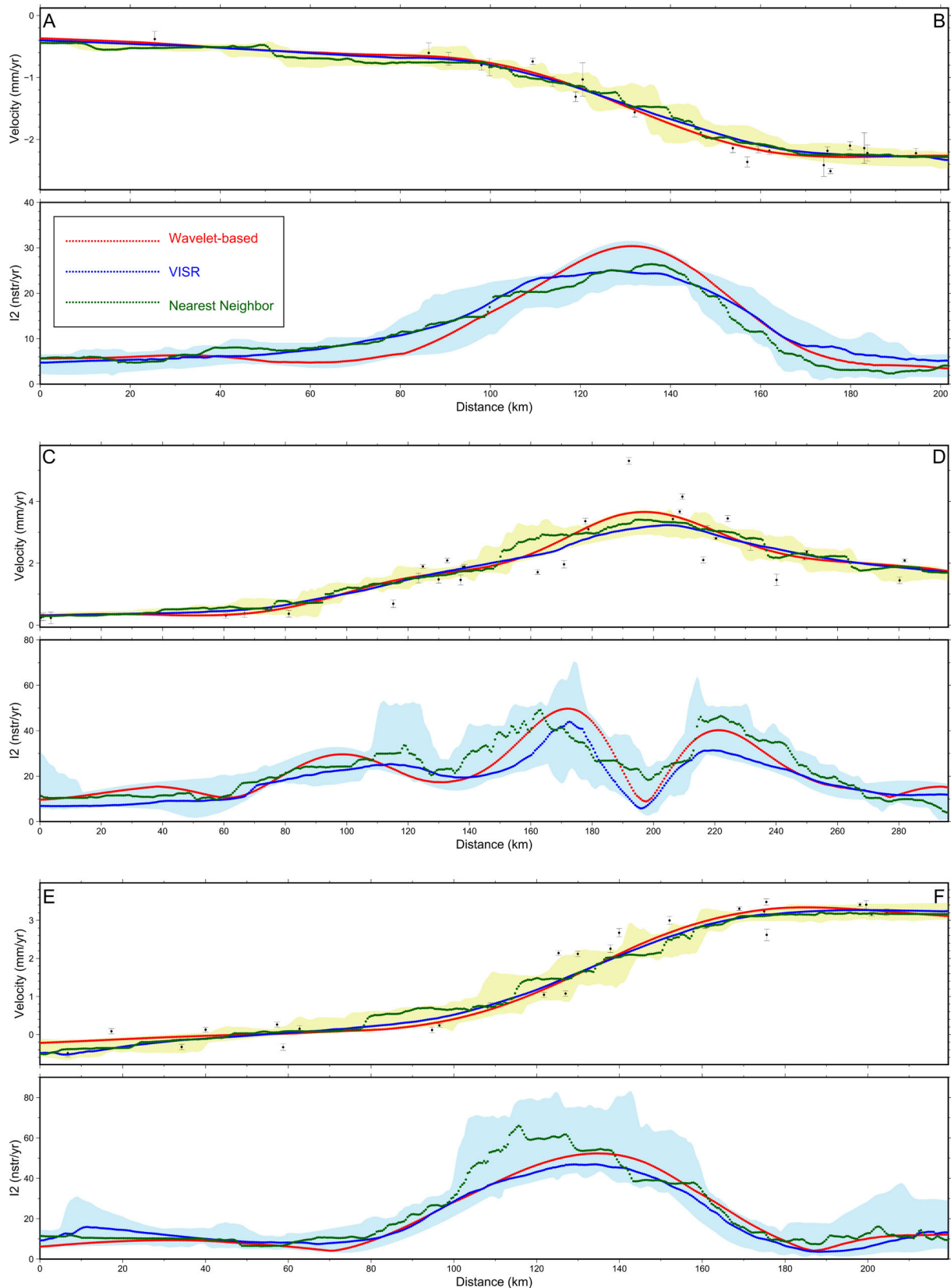
Figure 13. Profiles of the median velocity parallel to the track and median second invariant of the strain rate for the three methods (green: Nearest Neighbor approach, blue: VISR algorithm, red: Wavelet-based approach). Dots in the velocity profile represent along-track velocity data in a 50 km wide swath. Yellow and blue shadows represent an envelope of 95% of the total variability of the three methods for the velocity and the second invariant inside the swath.
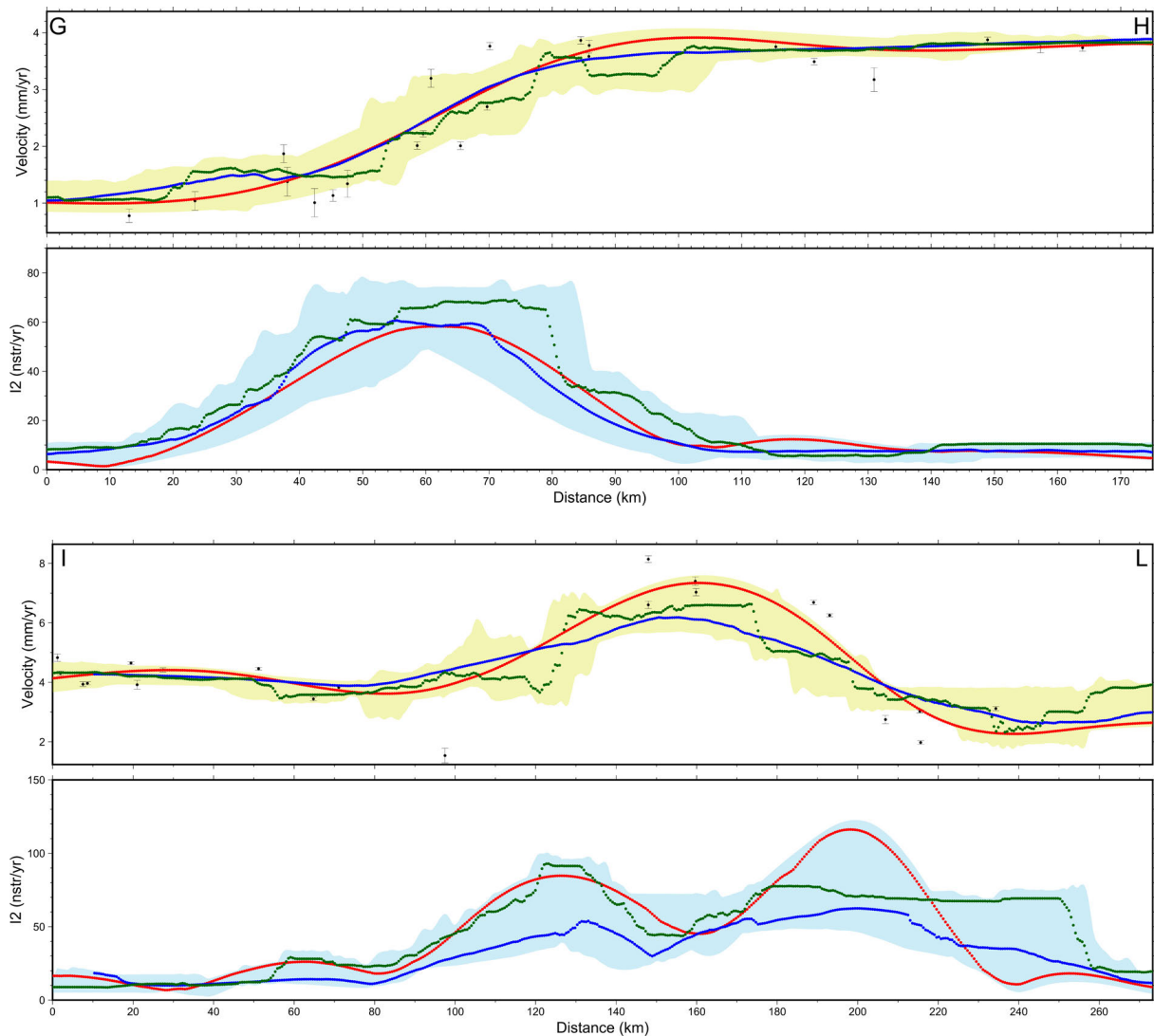
Figure 13.

Here, the maps point to minimal dilatation but a high deviatoric strain rate, while in eastern Tuscany, the strain rate diminishes but the second invariant is below the 30 nstr/yr.

Further to the south, strain rates drop significantly around the Pollino area, leveling off in Calabria and progressing towards Sicily via the Messina Strait. In northern Sicily, the models indicate an N-S extension, which transitions to N-S shortening in the southern Tyrrhenian, particularly around the central Aeolian Islands; both regions are characterized by high deformation rate values (above 60-70 nstr/yr but with disagreement between the methods).

Looking at the strain rate and modeled velocity profiles in Figure 13, some other common and different characteristics can be noticed:

– The AB profile, which crosses the South-Eastern Alps, indicates an increase in the magnitude of the parallel velocity as it crosses the mountain chain toward the Adriatic. This leads to contractional deformation [as observed by previous studies, e.g. Faccenna et al., 2014 and Sani et al., 2016], consistently shown across all three methods from very similar velocity profiles.

– The CD profile in northern Italy illustrates the profile parallel velocity's increase with variable slopes, before decreasing towards the Po Plain. This velocity variation causes three peaks of relatively higher deformation: one extensional peak on the Tyrrhenian side, another extensional peak in correspondence with the Apennine chain axis and a compressive one on the Adriatic side. This last peak is more pronounced in the Wavelet-based solution. The maximum magnitudes of the strain rate depend on the method used. The VISR solution estimates smaller amplitudes compared to the Wavelet-based and Nearest Neighbor methods. These differences probably reflect the differences in modeling the higher scatter of the GNSS velocities that occurs when crossing the Apennines.

- The EF and GH profiles in Central and Southern Apennines, show the parallel velocity peaking on the Adriatic side. Then, only one wide extensional deformation belt is apparent, which is consistently localized and determined by all three methods, even though the VISR and Wavelet-based solutions are in much closer agreement with each other than with the Nearest Neighbor solution, which typically shows higher variability and strain rate peaks.
- The IL profile in Eastern Sicily displays the modeled velocity increasing as it approaches the Tyrrhenian Sea, reaching its peak just before the transition to the sea. Subsequently, the velocity declines sharply, resulting in another pronounced peak in the strain rate, which is primarily compressive. Here, the methods lead to vastly different solutions having significant differences in the magnitude of the strain rate peaks. However, it seems that the Wavelet-based method is more capable of fitting the along-track velocities in the Tyrrhenian Sea compared to the other methods. This is also clear by looking at the residual map in Figure 10 where the residual velocities are more W-E directed compared to the residual velocities relative to the maps of the Nearest Neighbor and VISR methods (Figure 5 and Figure 8)

All solutions yield consistent results in identifying higher strain rate regions and provide estimates of the main axes of deformation with coherent and comparable directions. The observed principal directions of strain rate for the VISR method are also comparable with the principal directions of the strain rate products of EPOS [Fernandes et al., 2022]. The Nearest Neighbor method clearly provides the less smooth solution, with short wavelength changes in the modeled velocities, which map in rapid changes in the dilatational rates that do not necessarily reflect the scattered observed velocities. Conversely, VISR and Wavelet-based methods in general are in good agreement, although the most significant discrepancies are observed in Sicily and in the eastern part of the Calabrian Arc (here VISR and the Nearest Neighbor method highlight higher strain rate). This last effect is driven by stations with higher velocities in the Crotone area, which, as will be discussed in the next section, are likely affected by processes not related to tectonic activity.

5. Discussion

By definition, a model is an informative representation of reality; each modeling method has its pros and cons that should be considered when drawing conclusions from strain rate estimates, or when using those estimates for hazard assessment. The Nearest Neighbor approach has the advantage of being simpler than the other two methods discussed in this work since the strain rate estimate is only based on a certain number of neighboring GNSS stations. One main drawback of this approach is that the scale at which deformation is estimated is necessarily spatially variable since stations are not uniformly distributed in space. As observed by Maurer and Materna [2023], the spatial parameters should be adjusted based on the local station density. The VISR algorithm addresses this issue by weighting stations according to their spatial distribution, even if the prescribed scheme that describes how the stations are weighted is, to some extent, arbitrary. The Wavelet-based approach also accounts for the local station density, allowing for the identification of a minimum spatial scale of interest on which to compute the strain rate. This information on the spatial scale is encoded by the q_{max} parameter, which is intrinsically linked to the size of the wavelets used for estimating a continuous velocity field (from which the strain rate field is estimated). The main drawback in this case is that the choice of regularization of the inversion, based on ordinary cross-validation, is a function of the whole dataset. This implies that, even with the same q_{max}, the solution derived from a subset of a given data set may not match the one from the entire data set.

Overall, the three methods discussed in this work show features that are common to previous studies [e.g., Serpelloni et al., 2022, Sani et al., 2016, Faccenna et al., 2014 and D'Agostino, 2014]. The differences between solutions, to some extent, reflect the epistemic uncertainty related to strain rate estimates. A map depicting the differences between the second invariant of the strain rate, as estimated by the three methods, is shown in Figure 14.

Major differences in the strain rate maps can be summarized as follows:

- The Nearest Neighbor method shows greater discrepancies in the strain rate field compared to the others, especially in regions of central and southern Italy where the density of GNSS stations is high. This can be attributed to the fact that both the VISR and Wavelet-based methods weigh the contribution of each station based on the local station density while the Nearest Neighbor method does not. Consequently, they do not necessarily increase the estimated strain rate variability when spatially denser stations are considered.
- Significant differences are present in North-Eastern Sicily, especially when comparing the Wavelet-based and VISR methods, as evident from the IL profile in Figure 13. These discrepancies may arise due to the sparse spatial
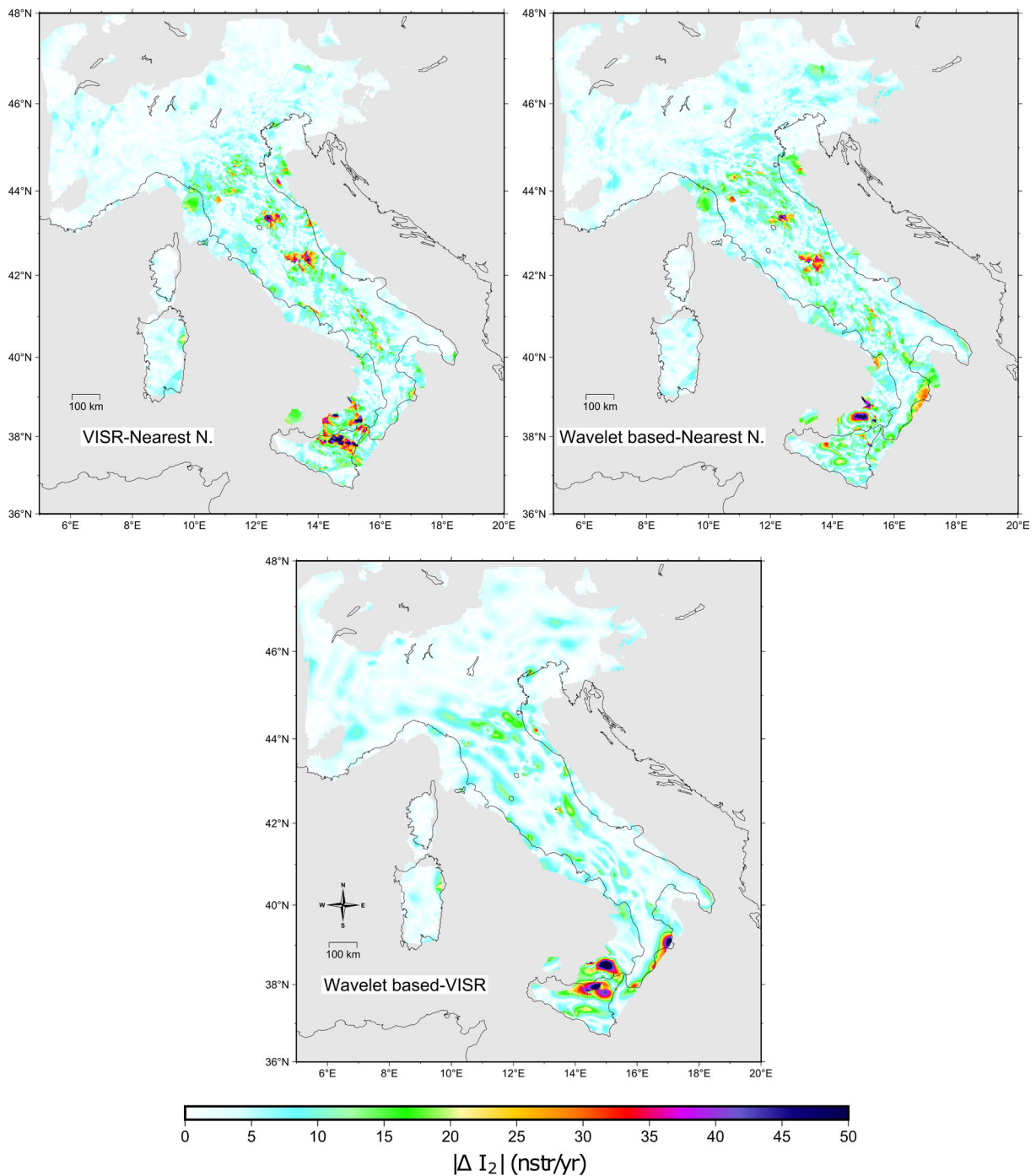
Figure 14. Absolute difference in the second invariant of the strain rate for each couple of methods.

distribution of the stations and their location on the edge of the GNSS stations network. It is noteworthy that the best fit for the higher velocities along the Sicilian coast is provided by the Wavelet-based method, resulting in higher strain rates.

– Notable differences in the strain rate fields are evident in the eastern part of the Calabrian arch when comparing the Nearest Neighbor and VISR methods to the Wavelet-based method. Both the Nearest Neighbor and VISR models point to increased rates on the eastern side of the Calabrian arc, as seen in Figure 12. However, we believe that these elevated rates might originate from factors other than tectonic activity, as suggested by D'Agostino et al., [2011]. These variations may be attributed to gravitational land movements, specifically discussed as megalandslide events in Minelli et al. [2013] and Zecchin et al. [2018]. Many GNSS stations in the Crotone region have likely been removed using the methods outlined in section 2.2. However, in this specific case,

automatic removal is complicated due to the coherent movement observed among stations in the region and the fact that this area lies at the edge of the GNSS network. To be more confident about the nature of the observed deformation, one might consider manually removing stations based on known models of the gravitational phenomenon. The Wavelet-based method, which is generally more robust in handling potential outliers, provides a strain rate field solution with significantly more modest rates compared to other approaches.

6. Conclusions

In this study, three methods of increasing mathematical complexity for the estimate of the geodetic strain rate are considered and compared. Strain rate maps representative of tectonic deformation rates are produced starting from a dense GNSS velocity dataset for Italy and its surroundings. The GNSS velocity field employed for the computation is filtered from stations that most likely respond to non-tectonic deformation processes, including volcanic and anthropogenic ones. This removal is mainly carried out through an automated process that is based on checking the coherence of each station with its neighbors. The methods employed to compute the geodetic strain rate fundamentally differ: Nearest Neighbor method computes the strain rate based on a certain number of nearby stations, the VISR method weights also the contribution of the stations based on their spatial distribution, the Wavelet-based method computes a continuous velocity field from which a strain rate field is derived. The arbitrariness on the setting of the parameters relative to each method is reduced by observing the Monte Carlo cross-validation curves, which represent a comparison between goodness of fit and parameter values, and the curves of the variability of the second invariant of the strain rate against the parameters. In every instance, the chosen solutions consistently identify regions with higher strain rates and offer estimates for the primary axes of deformation that have notably similar directions. In regions with a higher density of stations, the differences between the methods are more restrained, especially when comparing the maps from the VISR and Wavelet-based approaches, as both techniques consider a local station density of the GNSS stations. However, areas with sparsely distributed GNSS stations and a pronounced velocity gradient can result in notable discrepancies across all methods. Constructing diverse strain rate models and quantifying their differences is crucial for developing and testing robust seismic hazard models rooted in these strain rates. The strain-rate maps developed in this work will be used in a subsequent work that aims at developing seismicity rate models for the Apennines, adopting a procedure derived from Stevens and Avouac [2021], where different geodetic strain rate models will be used, together with different models for extracting catalogs of background seismicity, in order to provide earthquake recurrence models taking into account also the effects on the results of epistemic uncertainties in the modeling process.

References

Altamimi, Z., L. Métivier, P. Rebischung, H. Rouby and X. Collilieux (2017). ITRF2014 plate motion model, Geophys. J. Int. 209, 3, 1906-1912, doi: 10.1093/gji/ggx136.
Berrar, D. (2019). Cross-Validation, In: Encyclopedia of Bioinformatics and Computational Biology. Ed. by S. Ranganathan, M. Gribskov, K. Nakai and C. Schönbach. Oxford: Academic Press, 542-545. doi: https://doi.org/10.1016/B978-0-12-809633-8.20349-X.

Billi, A., M. Cuffaro, B. Orecchio, M. Palano, D. Presti and C. Totaro (2023). Retracing the Africa-Eurasia nascent convergent boundary in the western Mediterranean based on earthquake and GNSS data, Earth and Planet. Sci. Lett. 601, 117906, doi: https://doi.org/10.1016/j.epsl.2022.117906.

Blewitt, G., W.C. Hammond and C. Kreemer (2018). Harnessing the GPS Data Explosion for Interdisciplinary Science, Eos, 99, doi: https://doi.org/10.1029/2018EO104623.

D'Agostino, N. (2014). Complete seismic release of tectonic strain and earthquake recurrence in the Apennines (Italy), Geophys. Res. Lett. 41, 4, 1155-1162. doi: https://doi.org/10.1002/2014GL059230.

D'Agostino, N., E. D'Anastasio, A. Gervasi, I. Guerra, M.R. Nedimović, L. Seeber and M.L. Steckler (2011). Forearc extension and slow rollback of the Calabrian Arc from GPS measurements, Geophys. Res. Lett. 38, 17, doi: https://doi.org/10.1029/2011GL048270.

Devoti, R., N. D'Agostino, E. Serpelloni, G. Pietrantonio, F. Riguzzi, A. Avallone, A. Cavaliere, D. Cheloni, G. Cecere, C. D'Ambrosio, L. Franco, G. Selvaggi, M. Metois, A. Esposito, V. Sepe, A. Galvani and M. Anzidei (2017). A Combined Velocity Field of the Mediterranean Region, Ann. Geophys. 60, 2, doi: 10.4401/ag-7059.

England, P., G. Houseman and J.-M. Nocquet (2016). Constraints from GPS measurements on the dynamics of deformation in Anatolia and the Aegean, J. Geophys. Res.: Solid Earth, 121,12,8888-8916, doi: https://doi.org/10.1002/2016JB013382.

Faccenna, C., T.W. Becker, S.M. Miller, E. Serpelloni and S.D. Willett (2014). Isostasy, dynamic topography, and the elevation of the Apennines of Italy, Earth Planet. Sci. Lett., 407,163-174, doi: https://doi.org/10.1016/j.epsl.2014.09.027.

Fernandes, R., C. Bruyninx, P. Crocker, J.-L. Menut, A. Socquet, M. Vergnolle, A. Avallone, A.M. Bos, S. Bruni, R. Cardoso, L. Carvalho, N. Cotte, N. D'Agostino, A. Deprez, F. Andras, F. Geraldes, G. Janex, A. Kenyeres, J. Legrand, K.-M. Ngo, M. Lidberg, T. Liwosz, J. Manteigueiro, A. Miglio, W. Soehne, S. Holger, S. Toth, J. Dousa, A. Ganas, V. Kapetanidis and G. Batti (2022). A new European service to share GNSS Data and Products, Ann. Geophys, 65, 3, DM317, doi: 10.4401/ag-8776.

Golub, G.H. and C.F. Van Loan (1989). Matrix Computations, 2nd edn., Johns Hopkins Univ. Press, Baltimore, MD, USA.

Handwerger, A.L., M.H. Huang, E.J. Fielding, A.M. Bootj and R. Bürgmann (2019). A shift from drought to extreme rainfall drives a stable landslide to catastrophic failure, Sci. Rep., 9, 1569, doi: https://doi.org/10.1038/s41598-018-38300-0.

Masson, C., S. Mazzotti and P. Vernant (2019). Precision of continuous GPS velocities from statistical analysis of synthetic time series, Solid Earth, 10, 1, 329-342, doi: 10.5194/se-10-329-2019.

Mastrolembo Ventura, B., E. Serpelloni, A. Argnani, A. Bonforte, R. Bürgmann, M. Anzidei, P. Baldi and G. Puglisi (2014). Fast geodetic strain-rates in eastern Sicily (southern Italy): New insights into block tectonics and seismic potential in the area of the great 1693 earthquake, Earth Planet. Sci. Lett. 404, 77-88, doi:https://doi.org/10.1016/j.epsl.2014.07.025.

Materna, K. and J. Maurer (2023). Strain_2D (version 1.1.1), url: https://code.usgs.gov/kmaterna/Strain_2D.%20Archived%20at%20DOI:%2010. 5066/P9JJW0DY, https://github.com/kmaterna/Strain_2D.

Maurer, J. and K. Materna (2023). Quantification of geodetic strain rate uncertainties and implications for seismic hazard estimates, Geophys. J. Int., 234, 3, 2128-2142, doi: 10.1093/gji/ggad191.

Meletti, C, W. Marzocchi, V. D'Amico, G. Lanzano, L. Luzi, F. Martinelli, B. Pace, A. Rovida, M. Taroni, F. Visini and MPS.19 Working Group (2021). The new Italian Seismic Hazard Model (MPS19), Ann. Geophys., 64, 1, doi: 10.4401/ag-8579.

Minelli, L., A. Billi, C. Faccenna, A. Gervasi, I. Guerra, B. Orecchio and G. Speranza (2013). Discovery of a gliding salt-detached megaslide, Calabria, Ionian Sea, Italy, Geophys. Res. Lett. 40, 4220-4224, doi: 10.1002/grl.50818.

Pezzo, G., L. Petracchini, R. Devoti, R. Maffucci, L. Anderlini, I. Antoncecchi, A. Billi, E. Carminati, F. Ciccone, M. Cuffaro, M. Livani, M. Palano, P. Petricca, G. Pierantonio, F. Riguzzi, G. Rossi, F. Sparacino and C. Doglioni, C. (2020). Active fold-thrust belt to foreland transition in northern Adria, Italy, tracked by seismic reflection profiles and GPS offshore data.essing, Tectonics, 39, doi: https://doi.org/10.1029/2020TC006425.

Piña-Valdés, J., A. Socquet, C. Beauval, M.-P. Doin, N. D'Agostino and Z.-K. Shen (2022). 3D GNSS velocity field sheds light on the deformation mechanisms in Europe: Effects of the vertical crustal motion on the distribution of seismicity, J. Geophys. Res.: Solid Earth, 127, https://doi.org/10.1029/2021JB023451.

Sani, F., G. Vannucci, M. Boccaletti, M. Bonini, G. Corti and E. Serpelloni (2016). "Insights into the fragmentation of the Adria Plate, J. Geod. 102, 121-138, doi: https://doi.org/10.1016/j.jog.2016.09.004.

Serpelloni, E., A. Cavaliere, L. Martelli, F. Pintori, L. Anderlini, A. Borghi, D. Randazzo, S. Bruni, R. Devoti, P. Perfetti and S. Cacciaguerra (2022). Surface Velocities and Strain-Rates in the Euro-Mediterranean Region From Massive GPS Data Processing, Front. Earth Sci. 10, doi: 10.3389/feart.2022.907897.

Shen, Z.-K., M. Wang, Y. Zeng and F. Wang (2015). Optimal Interpolation of Spatially Discretized Geodetic Data, Bull. Seism. Soc. Am. 105, 4, 2117-2127, doi: 10.1785/0120140247.

Sparacino, F., M. Palano, J.A. Peláez and J. Fernández (2020). Geodetic Deformation versus Seismic Crustal Moment-Rates: Insights from the Ibero-Maghrebian Region, Remote Sens. 12,6, doi: 10.3390/rs12060952.

Stevens, V.L. and J.-P. Avouac (Mar. 2021). "On the relationship between strain rate and seismicity in the India-Asia collision zone: implications for probabilistic seismic hazard". In: Geophysical Journal International 226.1, pp. 220-245. issn: 0956-540X. doi: 10.1093/gji/ggab098, eprint: https://academic.oup.com/gji/article-pdf/226/1/220/43616725/ggab098.pdf, url: https://doi.org/10.1093/gji/ggab098.

Tape, C., P. Muse, M. Simons, D. Dong and F. Webb (2009). Multiscale estimation of GPS velocity fields, Geophys. J. Int., 179, 1681-1698, doi: 10.1111/j.1365-246X.2009.04337.x.

Wessel, P., J.F. Luis, L. Uieda, R. Scharroo, F. Wobbe, W.H.F. Smith and D. Tian (2019). The Generic Mapping Tools Version 6, Geochem., Geophys., Geosys. 20, 11, 5556-5564. doi: https://doi.org/10.1029/2019GC008515.

Zecchin, M., F. Accaino, S. Ceramicola, D. Civile, S. Critelli, C. Da Lio, G. Magnano, G. Prosser, P. Teatini and L. Tosi (2018). The Crotone Megalandslide, southern Italy: Architecture, timing and tectonic control, Scientific Rep. 8, doi: 10.1038/s41598-018-26266-y.

Zhao, K., M.A. Wulder, T. Hu, R. Bright, Q. Wu, H. Qin, Y. Li, E. Toman, B. Mallick, X. Zhang, X. and M. Brown (2019). Detecting change-point, trend, and seasonality in satellite time series data to track abrupt changes and nonlinear dynamics: A Bayesian ensemble algorithm, Remote Sens. Environ. 232, 111181, doi: https://doi.org/10.1016/j.rse.2019.04.034.

*CORRESPONDING AUTHOR: Riccardo NUCCI,

Department of Physics and Astronomy, University of Bologna, Italy

e-mail: riccardo.nucci4@unibo.it